solids

Article

Point-Defect Segregation and Space-Charge Potentials at the $\Sigma 5(310)[001]$ Grain Boundary in Ceria

Adrian L. Usler [†], **Henrik J. Heelweg** [†,‡], **Roger A. De Souza** [*] and **Annalena R. Genreith-Schriever** [§]

Institute of Physical Chemistry, RWTH Aachen University, 52074 Aachen, Germany;
usler@pc.rwth-aachen.de (A.L.U.); henrik.heelweg@rwth-aachen.de (H.J.H.);
annalena.genreith.schriever@rwth-aachen.de (A.R.G.-S.)
[*] Correspondence: desouza@pc.rwth-aachen.de
[†] These authors contributed equally to this work.
[‡] Current address: Department of Chemistry, Massachusetts Institute of Technology, Cambridge, MA 02139, USA.
[§] Current address: Yusuf Hamied Department of Chemistry, University of Cambridge, Cambridge CB2 1EW, UK.

Abstract: The atomistic structure and point-defect thermodynamics of the model $\Sigma 5(310)[001]$ grain boundary in CeO_2 were explored with atomistic simulations. An interface with a double-diamond-shaped structural repeat unit was found to have the lowest energy. Segregation energies were calculated for oxygen vacancies, electron polarons, gadolinium and scandium acceptor cations, and tantalum donor cations. These energies deviate strongly from their bulk values over the same length scale, thus indicating a structural grain-boundary width of approximately 1.5 nm. However, an analysis revealed no unambiguous correlation between segregation energies and local structural descriptors, such as interatomic distance or coordination number. From the segregation energies, the grain-boundary space-charge potential in Gouy–Chapman and restricted-equilibrium regimes was calculated as a function of temperature for dilute solutions of (i) oxygen vacancies and acceptor cations and (ii) electron polarons and donor cations. For the latter, the space-charge potential is predicted to change from negative to positive in the restricted-equilibrium regime. For the former, the calculation of the space-charge potential from atomistic segregation energies is shown to require the inclusion of the segregation energies for acceptor cations. Nevertheless, the space-charge potential in the restricted-equilibrium regime can be described well with an empirical model employing a single effective oxygen-vacancy segregation energy.

Keywords: CeO_2; grain boundary; structural width; segregation; structure–property relationship; acceptor doped; donor doped; space-charge potential

check for updates

Citation: Usler, A.L.; Heelweg, H.J.; De Souza, R.A.; Genreith-Schriever, A.R. Point-Defect Segregation and Space-Charge Potentials at the $\Sigma 5(310)[001]$ Grain Boundary in Ceria. *Solids* **2024**, *5*, 404–421. https://doi.org/10.3390/solids5030027

Academic Editor: Robert A. Jackson

Received: 11 June 2024
Revised: 26 July 2024
Accepted: 30 July 2024
Published: 3 August 2024

Copyright: © 2024 by the authors. Licensee MDPI, Basel, Switzerland. This article is an open access article distributed under the terms and conditions of the Creative Commons Attribution (CC BY) license (https://creativecommons.org/licenses/by/4.0/).

1. Introduction

The best solid-state ionic conductors generally consist of a highly conductive bulk phase and less conductive grain boundaries. Depending on a variety of factors—the specific material, its composition, and its thermal and chemical history—the diminished grain-boundary conductivity may stem from resistive impurity phases [1–3], from decreased charge-carrier concentrations in space-charge zones adjacent to the interface [4–10], or from the intrinsic structural resistance of the interface [11,12]. Improving the overall rate of ion transport in such materials requires the origin of the diminished grain-boundary conductivity to be identified and understood in detail.

One prototypical system in this regard is the oxide-ion conductor substituted CeO_2, a material utilised as an electrolyte in Intermediate Temperature Solid Oxide Fuel Cells (IT-SOFC) [13–16]. Initial work indicated that the diminished grain-boundary conductivity came from a second phase at the grain boundaries [17–20]. Later work on substantially purer samples found that even in the absence of impurity phases, low grain-boundary conductivity remained [21–23], and this effect was attributed to the presence of space-charge zones in which the ionic charge carriers (oxygen vacancies) are depleted [7,23]. Treating this phenomenon in a thermodynamic framework based on point-defect segregation requires space-charge layer formation to be driven by the segregation of oxygen vacancies from the bulk to the grain-boundary core. Indeed, such a model has been shown to describe quantitatively not only isothermal resistances for dilute [4,24,25] and concentrated compositions [8,26], but also resistances for a dilute composition as a function of temperature and oxygen partial pressure [27]. In addition, the model accounts for grain boundaries being oxygen-deficient [28–31] (they contain an excess of oxygen vacancies) and for the accumulation of acceptor dopants in the space-charge zones [28,30,31] (aliovalent species react to the electric field set up by the charged vacancies' redistribution from bulk to grain boundary). Furthermore, it also explains [32] why faster cation diffusion along grain boundaries, with an activation enthalpy close to that for bulk diffusion, is observed [33]. In all cases [4,8,24–27], quantitative modelling yielded an effective Gibbs segregation energy for oxygen vacancies to the grain boundaries of $\Delta_{\mathrm{seg}} g_{\mathrm{v}} = -(1 \text{ to } 2)$ eV. NB: the sign of the segregation energy is sometimes reversed in the literature (e.g., refs. [34,35]). We define $\Delta_{\mathrm{seg}} g_{\mathrm{def}} = \Delta_{\mathrm{f}} g^{\mathrm{gb}}_{\mathrm{def}} - \Delta_{\mathrm{f}} g^{\mathrm{b}}_{\mathrm{def}}$, i.e., as the difference in the Gibbs formation energy of a point defect between grain boundary and bulk, so that a negative segregation energy indicates a thermodynamic driving energy for defect segregation from the bulk to the grain boundary.

Atomistic simulation studies of selected grain boundaries in $\mathrm{CeO_2}$ [31,34,36–38] and other fluorite-related oxides [31,35,39–45] found that the boundaries are characterised not by a single site of preferential formation, as typically assumed in the thermodynamic model, but by a number of symmetry-inequivalent sites, each with its own specific segregation energy. Some sites exhibit a negative segregation energy ($\Delta_{\mathrm{seg}} u_{\mathrm{def}} < 0$), meaning that oxygen-vacancy segregation to these sites is thermodynamically favourable; other sites exhibit positive segregation energies; i.e., oxygen vacancies will preferably redistribute from these sites to the bulk. In addition, the studies indicate favourable segregation energies for acceptor dopants ($\Delta_{\mathrm{seg}} u_{\mathrm{a}} < 0$). Space-charge potentials have not yet been calculated from such simulation data ($\Delta_{\mathrm{seg}} u_{\mathrm{v}} < 0$, $\Delta_{\mathrm{seg}} u_{\mathrm{a}} < 0$), but it is clear that the segregation of acceptor cations cannot govern space-charge formation; otherwise, a negative space-charge potential (with accumulated oxygen vacancies in the space-charge zones) would result, and consequently, the experimentally observed hindrance of oxide-ion transport across boundaries would not be accounted for. The effect of combined $\Delta_{\mathrm{seg}} u_{\mathrm{v}} < 0$ and $\Delta_{\mathrm{seg}} u_{\mathrm{a}} < 0$ on the space-charge potential remains, therefore, to be elucidated.

The magnitude of the defect-segregation energies has been analysed in detail in previous studies [34,35,37,46,47] and different influences on the segregation energies have been discussed. In particular, the segregation energies of the cations have been analysed in terms of the mismatch between the ionic radius of the dopant and that of the host cation [34,35,46]. Besides this, bond lengths and coordination numbers in the boundary have also been claimed as important parameters [35,47]. However, no clear correlation between the segregation energies and these structural descriptors was found.

In addition to the question of the origin, there is the question of the grain-boundary width. This quantity, it is noted, can be defined in a number of ways [48]. The structural or crystallographic width refers to the finite distance over which the mismatch between two grains is accommodated [49]; the chemical width refers to the region over which the composition is different to the bulk composition [50–53]; the electrical width refers to distance obtained from impedance spectroscopy measurements [53,54]; and the diffusional width refers to the region along which diffusion may occur faster than in the bulk [27,55,56]. Here, we examine various methods to determine the structural width from atomistic simulations.

In this way, we come to the three main questions of this study: first, how the structural width of a grain boundary can be extracted from atomistic simulations; second, whether segregation energies can be related to local structural descriptors; and third, how a variety of segregation energies, for more than one point-defect species, affects the space-charge potential. To this end, we used Molecular Statics (MS) and Molecular Dynamics (MD) simulations to model the structure and the segregation thermodynamics of a grain boundary in CeO_2. Subsequently, we used Finite Element Method (FEM) calculations to obtain from the segregation energies the space-charge potential at the boundary as a function of temperature.

We chose the symmetric $\Sigma5(310)[001]$ tilt grain-boundary as a model system because the boundary is highly symmetric and has a small repeat unit, thus making it accessible to atomistic simulations. A variety of point defects may be present in varying concentrations in CeO_2, depending on the type and concentration of dopant, the temperature, and the oxygen partial pressure. Previous studies [57–59] indicated that in acceptor-doped systems, the dominant defects are oxygen vacancies (and, under reducing conditions, also electron polarons); in donor-doped systems, the dominant defects are electron polarons, and oxygen interstitials [60–62]. To probe defects on anion and cation sublattices, we therefore determined $\Delta_{\mathrm{seg}}u_{\mathrm{def}}$ for oxygen vacancies ($v_O^{\bullet\bullet}$), Sc and Gd acceptors (Sc'_{Ce} and Gd'_{Ce}), electron polarons (Ce'_{Ce}), and Ta donors ($Ta^{\bullet}_{Ce}$). (Defects are given in Kröger–Vink notation [63–65].)

2. Computational Methods

2.1. Atomistic Simulations

Atomistic simulations were based on the Born model of ionic solids [66], which treats ions as classical particles interacting through long-range electrostatic interactions and short-range parameterised Buckingham pair potentials (see Table 1) [67–69]. This description has been successfully applied to simulating CeO_2 in diverse cases [67,70–73]. Both Molecular Statics (MS) and Molecular Dynamics (MD) simulations were performed with the LAMMPS code [74]. Energy minimisations were performed at constant pressure $p = 0$; MD simulations were performed within the isothermal–isobaric (NpT) ensemble over simulation times of 3 ns.

Table 1. Parameters for the short-range Buckingham pair potentials.

Pair	A / eV	ρ / Å	C / (eV Å^6)	Ref.
$O^{2-} - O^{2-}$	22764.3	0.149	27.89	[67]
$Ce^{4+} - O^{2-}$	1986.83	0.35107	20.4	[67]
$Ce^{3+} - O^{2-}$	1731.61808	0.36372	14.43256	[67]
$Gd^{3+} - O^{2-}$	1336.8	0.3551	–	[68]
$Sc^{3+} - O^{2-}$	1299.4	0.3312	–	[68]
$Ta^{5+} - O^{2-}$	1315.572	0.36905	–	[69]

Using the GOSAM software (https://gosam.hepforge.org/) [75], we generated an initial grain-boundary supercell with 23,040 ions containing two anti-parallel $\Sigma5(310)[001]$ grain boundaries. This involved the rotation of two fluorite-structured ($Fm\bar{3}m$) ceria grains around the $[001]$ axis by $\theta = 36.9°$, so that their (310) planes coincided. Subsequently, we performed three-dimensional rigid-body translations of the two grains, i.e., we shifted the grains relative to one another in steps of 1 Å, and performed at each step an energy optimisation, in this way scanning the so-called γ-surface. For each configuration, we then carried out a high-temperature anneal (at $T = 2000\,\mathrm{K}$) in an MD simulation, followed by a final static energy optimisation. The grain-boundary structure with the lowest energy is shown in Figure 1. The corresponding supercell had dimensions of ca. 65.3 Å × 68.7 Å × 70.3 Å; the two anti-parallel boundaries are thus separated by a distance of $d_{\mathrm{gb-gb}} = 35.1$ Å. This grain-boundary simulation cell was employed in a previous communication [12].

We found scanning the γ-surface and a sufficiently high temperature in the MD run to be decisive for obtaining the low-energy configuration. We recommend, as other authors have [76], a three-step procedure involving first scanning the γ-surface; subsequently carrying out a high-temperature MD run for each rigid body translation over extended simulation times; and finally conducting a static energy minimisation. In particular, we emphasise the need to use sufficiently large cells, and to combine different techniques to obtain the minimum-energy configuration.

A single point defect was then introduced at various symmetry-inequivalent positions in the supercell (its charge being compensated by a uniform background charge), and all ion positions were subsequently relaxed (at constant volume) to zero net force with a steepest-descent algorithm. The defect formation energies ($\Delta_\mathrm{f} u_\mathrm{def}$) were determined at all positions at zero Kelvin.

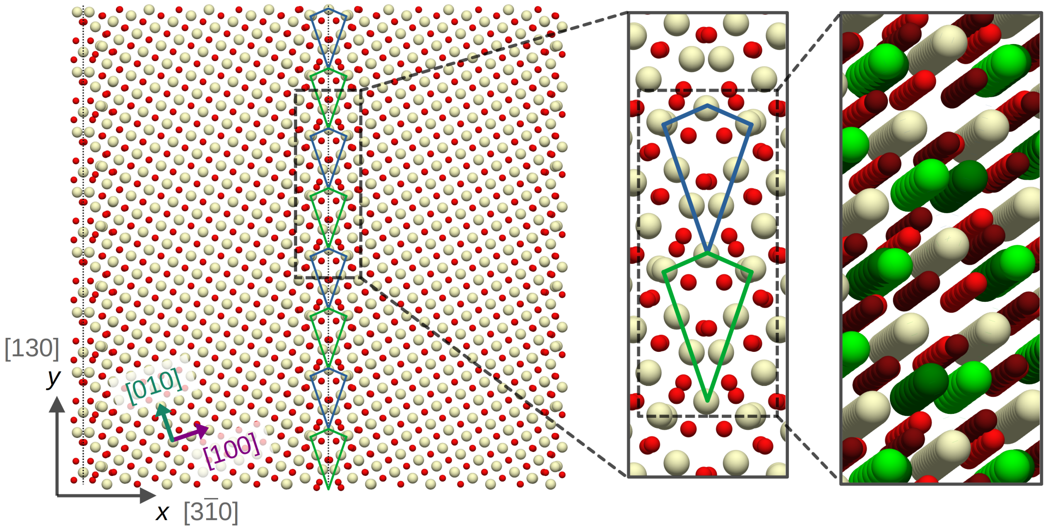

Figure 1. Simulation supercell with two anti-parallel $\Sigma5(310)[001]$ grain boundaries, one at the centre of the cell and one half at each edge, viewed along the [001] axis (corresponding to the *z* direction of the simulation cell), visualised with the MOLARA package [77]. The light-yellow spheres denote cerium ions, and the red spheres, oxide ions. The closeups show the characteristic structural motif, which has a double-diamond shape, as indicated by the blue and green sketched diamonds; the ions occupy alternating positions both along *x* and *y* directions. In the closeup on the right, the alternating cerium positions are highlighted in light green and dark green; and the alternating oxygen positions are highlighted in light red and dark red.

2.2. Structural Analysis

We take as structural descriptors the nearest-neighbour distances around the respective site ($d_\mathrm{min}^\mathrm{Ce\text{–}Ce}$, $d_\mathrm{min}^\mathrm{Ce\text{–}O}$, $d_\mathrm{min}^\mathrm{O\text{–}Ce}$, $d_\mathrm{min}^\mathrm{O\text{–}O}$), and a modified version of the Effective Coordination Number (ECoN) [78,79]. We introduced a modified ECoN in order to make it more resilient against the strong structural distortions in grain-boundary regions: in these regions, distortions may be severe, and the smallest interatomic distance will generally dominate the average coordination distance, d_avg. That is, a particle might be identified as being outside of the coordination environment if other particles are even closer, even if the same distance would be well within the coordination environment in the bulk phase. Hence, before calculating coordination distances and numbers for the simulation cell as a whole, we calculated an average coordination distance d_avg for the particles in the bulk phase.

The average coordination distance for a given site, d_avg^s, is obtained by iteratively solving as follows:

$$d_\mathrm{avg}^s = \frac{\sum\limits_j d_{js} \exp\left[1 - \left(\frac{d_{js}}{d_\mathrm{avg}^s}\right)^6\right]}{\sum\limits_j \exp\left[1 - \left(\frac{d_{js}}{d_\mathrm{avg}^s}\right)^6\right]} =: \frac{\sum_j d_{js}\, w_{js}}{\sum_j w_{js}}, \qquad (1)$$

where d_{js} denotes the distance between site j and site s, and w_{js} is short for the exponential weight based on said distance. In the original approach by Hoppe [78,79], the ECoN is then obtained as $\mathrm{ECoN}(s) = \sum_j w_{js}$. For the reasons laid out above, we take mean values of the bulk-phase distances from Equation (1) as a reference, instead of using the interatomic distances for each site individually. The use of fixed reference distances implies, however, that particles closer than the reference distance could be counted as multiple particles in the ECoN. To avoid this, we apply a cutoff value of 1 to the weights. With this, the modified weight terms $w_{js,\,\mathrm{mod}}$ read

$$w_{js,\,\mathrm{mod}} = \min\left\{1,\ \exp\left[1 - \left(\frac{d_{js}}{d_{\mathrm{avg}}^{\mathrm{ref}}}\right)^{6}\right]\right\}, \tag{2}$$

where $d_{\mathrm{avg}}^{\mathrm{ref}}$ stands for the appropriate reference coordination distances ($d_{\mathrm{avg}}^{\mathrm{Ce\text{–}Ce}}$, $d_{\mathrm{avg}}^{\mathrm{Ce\text{–}O}}$, $d_{\mathrm{avg}}^{\mathrm{O\text{–}Ce}}$, or $d_{\mathrm{avg}}^{\mathrm{O\text{–}O}}$). From this, we calculate the modified effective coordination number:

$$\mathrm{ECoN}_{\mathrm{mod}} = \sum_{j} w_{js}^{*}. \tag{3}$$

For the sake of a manageable computational cost, the summations in Equations (1) and (3) were only carried out over the neighbouring particles within 7 Å of the respective site. The neighbouring particles within the cutoff radius were identified with k-d-tree search algorithms [80] from the SciPy package [81] for Python. A detailed comparison of the original ECoN approach with other definitions of a coordination number can be found in ref. [82].

2.3. Continuum Modelling of Space-Charge Layers

The calculation of the space-charge potential employs a one-dimensional continuum approach, and it is based on the electrochemical potential of a defect building unit in the bulk and in the grain-boundary [6] taking the form

$$\eta_{\mathrm{def}} = \Delta_{\mathrm{f}} g_{\mathrm{def}} + k_{\mathrm{B}} T \,\ln\!\left(\frac{n_{\mathrm{def}}}{1 - n_{\mathrm{def}}}\right) + z_{\mathrm{def}}\, e\, \phi, \tag{4}$$

with $\Delta_{\mathrm{f}} g_{\mathrm{def}}$ denoting the Gibbs formation energy and z_{def} the charge number of the point defect on the specific type of site (note that $\Delta_{\mathrm{f}} g_{\mathrm{def}}$ is also referred to as the standard chemical potential $\mu_{\mathrm{def}}^{\ominus}$ in the literature). Defect–defect interactions are neglected. Defect concentrations are treated in terms of site fractions n (n_{v} for $\mathrm{v}_{\mathrm{O}}^{\bullet\bullet}$; n_{a} for $\mathrm{Acc}_{\mathrm{Ce}}^{\prime}$; n_{e} for $\mathrm{Ce}_{\mathrm{Ce}}^{\prime}$; n_{d} for $\mathrm{Ta}_{\mathrm{Ce}}^{\bullet}$).

In electrochemical equilibrium [$\eta_{\mathrm{def}}(x) = \eta_{\mathrm{def}}^{\mathrm{b}}$], the site fractions are thus directly related to the electric potential. In the case of acceptor-doped $\mathrm{CeO_2}$, we ignore that $\mathrm{CeO_2}$ will be reduced (i.e., will contain electron polarons) at very high temperatures, even in oxidising conditions; bulk electroneutrality is therefore approximated by $4\,n_{\mathrm{v}} = n_{\mathrm{a}}$. For the space-charge zones, we thus take into account the site fractions of $\mathrm{v}_{\mathrm{O}}^{\bullet\bullet}$ and $\mathrm{Acc}_{\mathrm{Ce}}^{\prime}$:

$$n_{\mathrm{v}} = \frac{n_{\mathrm{v}}^{\mathrm{b}}\, \mathrm{e}^{-\beta\,(\Delta_{\mathrm{seg}} g_{\mathrm{v}} + 2e\,\phi)}}{1 + n_{\mathrm{v}}^{\mathrm{b}}\left[\mathrm{e}^{-\beta\,(\Delta_{\mathrm{seg}} g_{\mathrm{v}} + 2e\,\phi)} - 1\right]}, \tag{5}$$

$$n_{\mathrm{a}} = \frac{n_{\mathrm{a}}^{\mathrm{b}}\, \mathrm{e}^{-\beta\,(\Delta_{\mathrm{seg}} g_{\mathrm{a}} - e\,\phi)}}{1 + n_{\mathrm{a}}^{\mathrm{b}}\left[\mathrm{e}^{-\beta\,(\Delta_{\mathrm{seg}} g_{\mathrm{a}} - e\,\phi)} - 1\right]}, \tag{6}$$

with $\beta := 1/(k_{\mathrm{B}} T)$. Note that in Equations (5) and (6), we implicitly set the reference value ϕ^{b} of the electric potential to zero. In the donor-doped case, we approximate the bulk defect chemistry with $n_{\mathrm{d}} = n_{\mathrm{e}}$; that is, we ignore the concentration of oxygen interstitials.

Here, the electrochemical potentials have a slightly different form to that of Equation (4), to account for electron polarons and donor cations sharing the same sublattice:

$$\eta_{\mathrm{e}} = \Delta_{\mathrm{f}} g_{\mathrm{e}} + k_{\mathrm{B}} T \, \ln\left(\frac{n_{\mathrm{e}}}{1 - n_{\mathrm{e}} - n_{\mathrm{d}}} \right) - e\,\phi, \tag{7}$$

$$\eta_{\mathrm{d}} = \Delta_{\mathrm{f}} g_{\mathrm{d}} + k_{\mathrm{B}} T \, \ln\left(\frac{n_{\mathrm{d}}}{1 - n_{\mathrm{e}} - n_{\mathrm{d}}} \right) + e\,\phi, \tag{8}$$

and with that, the site fractions of electron polarons and donor cations in the Gouy–Chapman regime read

$$n_{\mathrm{e}} = \frac{n_{\mathrm{e}}^{\mathrm{b}}\, \mathrm{e}^{-\beta\,(\Delta_{\mathrm{seg}} g_{\mathrm{e}} - e\,\phi)}}{1 + n_{\mathrm{e}}^{\mathrm{b}} \left[\mathrm{e}^{-\beta\,(\Delta_{\mathrm{seg}} g_{\mathrm{e}} - e\,\phi)} - 1 \right] + n_{\mathrm{d}}^{\mathrm{b}} \left[\mathrm{e}^{-\beta\,(\Delta_{\mathrm{seg}} g_{\mathrm{d}} + e\,\phi)} - 1 \right]} \tag{9}$$

$$n_{\mathrm{d}} = \frac{n_{\mathrm{d}}^{\mathrm{b}}\, \mathrm{e}^{-\beta\,(\Delta_{\mathrm{seg}} g_{\mathrm{d}} + e\,\phi)}}{1 + n_{\mathrm{e}}^{\mathrm{b}} \left[\mathrm{e}^{-\beta\,(\Delta_{\mathrm{seg}} g_{\mathrm{e}} - e\,\phi)} - 1 \right] + n_{\mathrm{d}}^{\mathrm{b}} \left[\mathrm{e}^{-\beta\,(\Delta_{\mathrm{seg}} g_{\mathrm{d}} + e\,\phi)} - 1 \right]}. \tag{10}$$

In the restricted-equilibrium regime (the donor-cation profile being fixed to $n_{\mathrm{d}}^{\mathrm{crit}}$), the expression for the site fraction of polarons reads

$$n_{\mathrm{e}} = \frac{n_{\mathrm{e}}^{\mathrm{b}}\, \mathrm{e}^{-\beta\,(\Delta_{\mathrm{seg}} g_{\mathrm{e}} - e\,\phi)}\,(1 - n_{\mathrm{d}}^{\mathrm{crit}})}{1 - n_{\mathrm{d}}^{\mathrm{b}} + n_{\mathrm{e}}^{\mathrm{b}} \left[\mathrm{e}^{-\beta\,(\Delta_{\mathrm{seg}} g_{\mathrm{e}} - e\,\phi)} - 1 \right]}. \tag{11}$$

We assume $\Delta_{\mathrm{seg}} g_{\mathrm{def}} \approx \Delta_{\mathrm{seg}} u_{\mathrm{def}}$, so that the segregation energies from the atomistic simulations can be used as the thermodynamic driving energies. Outside of the grain-boundary region, all sites are symmetry-equivalent, with $\Delta_{\mathrm{seg}} g_{\mathrm{def}} = 0$ by definition. In the acceptor-doped case, the Poisson equation reads

$$-\epsilon_{\mathrm{r}}\,\epsilon_0\,\frac{\mathrm{d}^2\phi}{\mathrm{d}x^2} = 2e\,\gamma_{\mathrm{O}}\,n_{\mathrm{v}} - e\,\gamma_{\mathrm{Ce}}\,n_{\mathrm{a}}, \tag{12}$$

and in the donor-doped case,

$$-\epsilon_{\mathrm{r}}\,\epsilon_0\,\frac{\mathrm{d}^2\phi}{\mathrm{d}x^2} = e\,\gamma_{\mathrm{Ce}}\,(n_{\mathrm{d}} - n_{\mathrm{e}}), \tag{13}$$

with the site densities γ_{O} and γ_{Ce} of oxygen and cerium sites, respectively, being calculated from the lattice constant a as

$$\gamma_{\mathrm{O}} = 2\,\gamma_{\mathrm{Ce}} = 8a^{-3}. \tag{14}$$

We assume that the variation in the electric potential is small within the grain-boundary core region, so that it is sufficient to treat the grain boundary as a plane rather than a region of finite width, with the amount of charge per unit area being the key quantity. This areal charge density is calculated from the core-site occupancies and the areal grain-boundary site densities, Γ_{O} and Γ_{Ce}. In the given grain-boundary structure, there are two equivalent sites in every structural motif (owing to screw symmetry at the grain-boundary plane). That is, every single type of site has the same density of sites per unit area (but the areal density of oxygen sites differs from that of cerium sites; $\Gamma_{\mathrm{O}} = 2\,\Gamma_{\mathrm{Ce}}$). The areal charge density in the grain-boundary core, Q^{c}, is taken into account by a Neumann boundary condition at the left edge of the simulation cell ($x = 0$), where the grain boundary is located:

$$-\epsilon_{\mathrm{r}}\,\epsilon_0\,\left.\frac{\partial\phi}{\partial x}\right|_{x=0} = \frac{1}{2}\cdot Q^{\mathrm{c}}. \tag{15}$$

In the acceptor-doped case, Q^{c} is calculated as

$$Q^{\mathrm{c}} = 2e\,\Gamma_{\mathrm{O}} \sum_{\text{O sites}} n_{\mathrm{v}} - e\,\Gamma_{\mathrm{Ce}} \sum_{\text{Ce sites}} n_{\mathrm{a}}, \tag{16}$$

and in the donor-doped case,

$$Q^{\mathrm{c}} = e\,\Gamma_{\mathrm{Ce}} \sum_{\text{Ce sites}} (n_{\mathrm{d}} - n_{\mathrm{e}}), \tag{17}$$

with n_{v}, n_{a}, n_{d}, and n_{e} being calculated with Equations (5)–(11). Parameters for the continuum simulations are given in Table 2.

Table 2. Simulation parameters for the FEM simulations of the space-charge layers.

Symbol	Value	Comment
$n_{\mathrm{a}}^{\mathrm{b}}$	10^{-3}	bulk doping level
$a/\text{Å}$	5.45	lattice constant [83]
ϵ_{r}	60	rel. diel. permittivity [84]
Γ_{O}	4.282×10^{18}	areal core O-site density
Γ_{Ce}	2.141×10^{18}	areal core Ce-site density

3. Results

Figure 1 shows the atomistic structure of the grain boundary, obtained through a combination of static and dynamic simulation methods, as described above. The characteristic structural unit has a double-diamond shape with ion positions alternating in all three dimensions. In previous studies of this boundary in CeO_2, UO_2, and cubic ZrO_2, only the single-diamond motive was considered in many cases [40,42,43,45], and in studies that appear to have found the double-diamond repeat unit [34,38,39,44], this more complex repeat unit has not been identified. In our study, we find the double-diamond structure (referring to the highlighted geometry within the box in the middle of Figure 1) to show the lowest energy. Evidently, such a structure may be obtained only in a sufficiently large simulation box, i.e., the box length must be some multiple of the double-diamond repeat unit. The excess energy of this grain boundary is $\Delta_{\mathrm{f}}E_{\mathrm{gb}} = 2.85\,\mathrm{J\,m^{-2}}$; and its excess volume is $\Delta_{\mathrm{f}}V_{\mathrm{gb}} = 0.9$ Å^3 Å^{-2}. Note that this grain-boundary structure may be specific to CeO_2 and the interatomic potentials used. Literature values [38,45,85] for this boundary are of the same order of magnitude, but are not strictly comparable, since they refer to other fluorite oxides, and to results obtained with other methods.

When a point defect is introduced into a grain-boundary supercell, its formation energy is expected to show different values within the grain-boundary regions, on account of the altered structure there. At sufficiently large distances from the two boundary planes, i.e., in the bulk region, the energy should assume a constant value (unless there is a non-zero electric field within the bulk part of the simulation cell [86]). This behaviour is observed, satisfyingly, for all point defects examined. We show in Figure 2 the segregation energies at different sites within the simulation cell, as well as the nearest-neighbour distances (with regard to the counter ions) and modified effective coordination numbers $\mathrm{ECoN_{mod}}$. More specifically, atomic sites are clearly bulk-like if they are more than 1 nm away from the grain-boundary planes. It is also evident that, for all considered defects, the energies in the vicinity of the grain boundaries (within 7.5 Å distance) deviate substantially from their bulk values. The precise choice of a cutoff between these regions (i.e., the structural width), however, is to some degree arbitrary. As can be seen in Figure 2b,c, there are only subtle deviations of the interatomic distances and coordination numbers from their bulk values in the transition regions. This indicates that the defect-formation energy reacts quite sensitively even to minor structural distortions. Here, considering all the information together, we take a distance of 7.5 Å on either side of the boundary plane, and thus obtain a structural grain-boundary width of ca. 1.5 nm. Since this way of estimating a structural width is based upon the spatial profiles of the segregation energies, the obtained width may also be identified as the width of the grain-boundary core in a space-charge model. While the extent of the structural perturbation may vary, to some degree, between different grain-boundary types, it may generally be expected to be of the order of a few lattice constants.

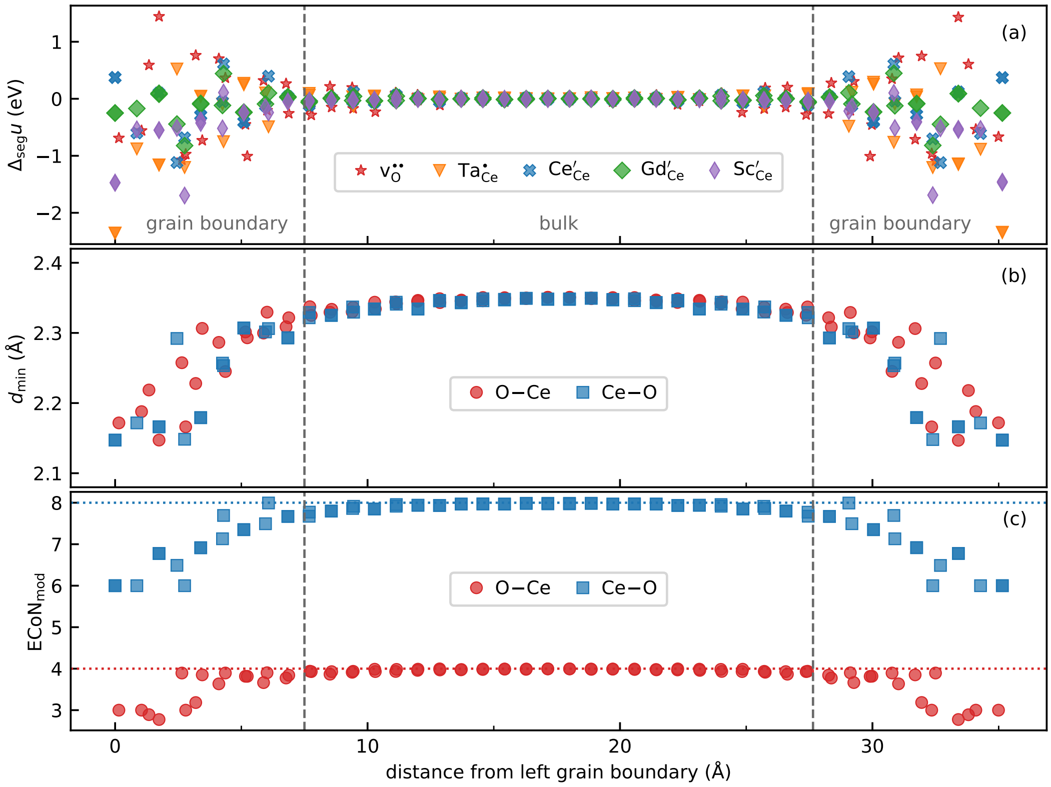

Figure 2. Microscopic properties across the simulation cell as a function of the distance from the left grain boundary. (**a**) Segregation energies of different point-defect species; (**b**) nearest-neighbour distances d_{min}, calculated from the structure of a cell devoid of point defects; (**c**) modified effective coordination numbers ($\mathrm{ECoN_{mod}}$), calculated with Equation (3) from the simulation cell without point defects. The regions within 7.5 Å distance from the grain-boundary planes are identified as the grain-boundary core regions.

As in earlier studies [34,35], both negative and positive segregation energies in the grain-boundary regions are found, that is, driving energies for defect segregation from the bulk to the boundary, and vice-versa. Although both sets of values are important in deriving relationships between structure and energetics (see below), only the negative values are important for space-charge formation [6], since, in a dilute solution, only these favourable energies produce substantial changes in the grain-boundary charge. And here one finds, as the most negative values, $\Delta_{\mathrm{seg}}u_{\mathrm{v}} = -1.1\,\mathrm{eV}$, $\Delta_{\mathrm{seg}}u_{\mathrm{e}} = -1.1\,\mathrm{eV}$, $\Delta_{\mathrm{seg}}u_{\mathrm{d}}^{\mathrm{Ta}} = -2.4\,\mathrm{eV}$, $\Delta_{\mathrm{seg}}u_{\mathrm{a}}^{\mathrm{Sc}} = -1.7\,\mathrm{eV}$, and $\Delta_{\mathrm{seg}}u_{\mathrm{a}}^{\mathrm{Gd}} = -0.8\,\mathrm{eV}$.

3.1. Analysing the Correlations between Local Structure and Segregation Energies

The defect formation energies differ from their bulk values in an extended region around the grain-boundary plane, with most changes occurring in the region up to 7.5 Å but bulk behaviour only being attained at a distance of ca. 10 Å (see Figure 2). That is, grain-boundary segregation to and from the boundary region must be considered to occur for a multitude of inequivalent sites. In Figure 3, we show the trend of the segregation energies on all inequivalent grain-boundary sites, with the nearest-neighbour distances $d_{\mathrm{min}}^{\mathrm{Ce\text{–}O}}$ indicated by a colour code. While some sites show a monotonous increase in $\Delta_{\mathrm{seg}}u$

with ionic radius, and others go through a maximum, there are also cases with a steady decrease in $\Delta_{\mathrm{seg}}u$.

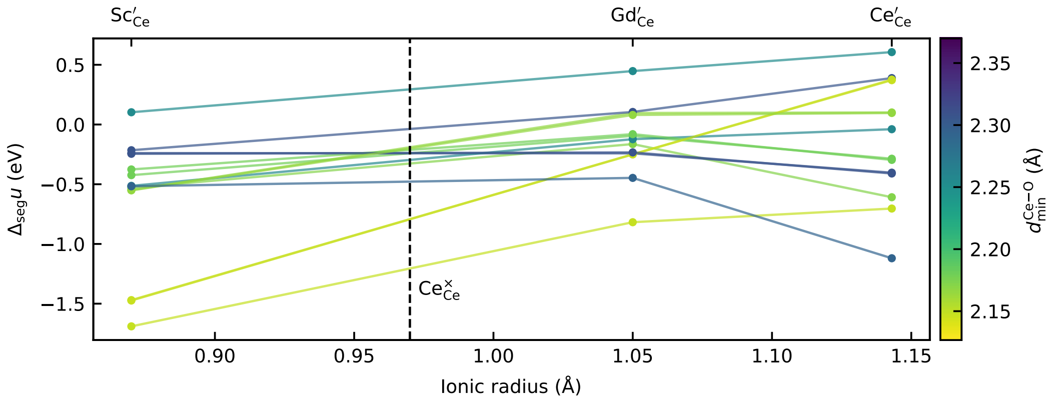

Figure 3. Segregation energies $\Delta_{\mathrm{seg}}u_{\mathrm{def}}$ for three substitutional cation defects with a single negative relative charge plotted against the cations' ionic radii as tabulated (Shannon [87]) for six-fold coordination. The colour code indicates the nearest-neighbour distance $d^{\mathrm{Ce–O}}_{\mathrm{min}}$ at the respective site.

Two grain-boundary sites exhibit a particularly pronounced increase of $\Delta_{\mathrm{seg}}u$ with the ionic radius; as indicated by the colour code in Figure 3, these sites also exhibit the shortest nearest-neighbour distances. The trends on these two sites suggest that, in line with arguments made in earlier studies [46], sites with short interatomic distances are particularly suitable for accommodating a negative size mismatch, i.e., the impurity cation being smaller than the $\mathrm{Ce}^{\times}_{\mathrm{Ce}}$ host cation.

In some instances [88,89], the ionic size mismatch has been discussed as though it were interchangeable with the segregation bias. Our results demonstrate that this perspective is unsuitable, both quantitatively and qualitatively: the interatomic distances are generally smaller in the grain boundary than in the bulk. Hence, if the segregation energies were determined by the ionic size mismatch alone, all $\mathrm{Sc}'_{\mathrm{Ce}}$ segregation energies would need to be negative, and all $\mathrm{Ce}'_{\mathrm{Ce}}$ segregation energies positive. More than that, the $\mathrm{Gd}'_{\mathrm{Ce}}$ segregation energies would, on all sites, have to be smaller in magnitude than the corresponding segregation energies for $\mathrm{Sc}'_{\mathrm{Ce}}$ and $\mathrm{Ce}'_{\mathrm{Ce}}$. Clearly, this rationale misrepresents the systematics of point-defect segregation observed here.

In an earlier study [88], it was proposed that the systematics of the point-defect segregation energies should be described by a quadratic dependence of the segregation energy on the ionic size mismatch, based on continuum elasticity theory [90]. A similar dependence has been suggested for the average of the segregation energies at a grain boundary [34]. In that regard, it should first be noted that the (arithmetic) average of segregation energies is not a meaningful measure. In a space-charge model, the effects of a very positive and a very negative segregation energy will not cancel each other out. Rather, the negative segregation energy will dominate the behaviour, as we will demonstrate in the following section. Second, it is to be noted that Figure 3 indicates quite clearly that some sites show a qualitatively different behaviour ($\Delta_{\mathrm{seg}}u_{\mathrm{def}}$ exhibiting a monotonous increase or decrease, rather than a maximum). An approach that only takes the ionic size mismatch as a measure disregards the influence of the geometry at the specific grain-boundary site. Not every site will equally well accommodate either a negative or a positive size mismatch.

We therefore show in Figure 4 how the segregation energies of $\mathrm{v}^{\bullet\bullet}_{\mathrm{O}}$, $\mathrm{Ta}^{\bullet}_{\mathrm{Ce}}$, $\mathrm{Sc}'_{\mathrm{Ce}}$, $\mathrm{Gd}'_{\mathrm{Ce}}$, and $\mathrm{Ce}'_{\mathrm{Ce}}$ depend on the nearest-neighbour distance of the counter ions. While, for $\mathrm{Sc}'_{\mathrm{Ce}}$ and $\mathrm{Ta}^{\bullet}_{\mathrm{Ce}}$ ions, there appears to be a weak positive correlation between $\Delta_{\mathrm{seg}}u$ and $d^{\mathrm{Ce–O}}_{\mathrm{min}}$, no clear trends are discernible for $\mathrm{v}^{\bullet\bullet}_{\mathrm{O}}$, $\mathrm{Ce}'_{\mathrm{Ce}}$, and $\mathrm{Gd}'_{\mathrm{Ce}}$. Similarly, the segregation energies show no clear correlation on the $\mathrm{ECoN}_{\mathrm{mod}}$ (not shown). This indicates that the segregation energies are not determined simply by the local environment around a site. As we will see in the next section, oxygen vacancies play the key role in determining the space-charge potential. It is, therefore, particularly striking that no clear trend may be formulated for their segregation energies, since it suggests that macroscopic grain-boundary properties cannot be related to these microscopic structural descriptors.

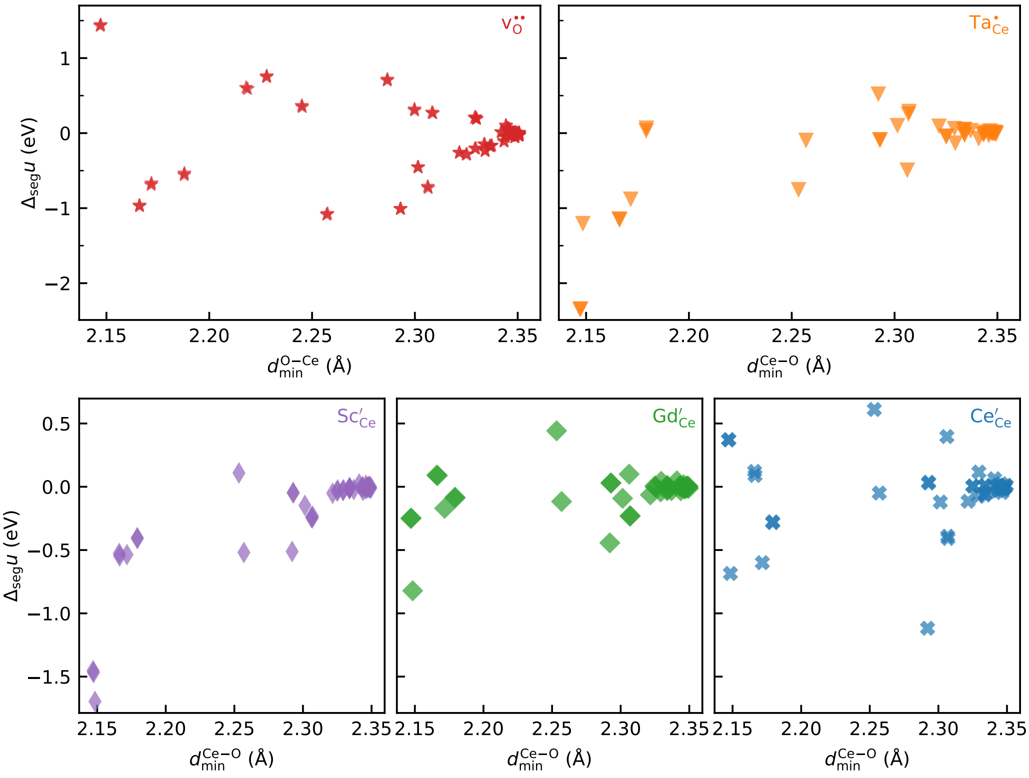

Figure 4. Segregation energies $\Delta_{seg}u_{def}$ as a function of the nearest-neighbour distance of the counter ions, i.e., $d_{min}^{O–Ce}$ in the case of $v_O^{\bullet\bullet}$, and $d_{min}^{Ce–O}$ in the case of the cation defects.

One further influence that must be taken into account is the lower charge number (3+) of the acceptor cations and electron polarons. The interplay of this charge difference with the altered coordination environment in the grain-boundary region will also contribute to the segregation energy [85]. In other words, trying to obtain a quantitative, universal structure–property relationship (based on simple, local descriptors) appears to be impossible, even for this simple, highly symmetric, tilt grain boundary.

3.2. The Effects of Different Segregation Energies on Space-Charge Behaviour

Having looked in more detail at the origin of point-defect segregation, let us now turn to its effects, i.e., the formation of space-charge zones. We calculated the space-charge potential Φ_0 as a function of temperature for (i) the case of a dilute solution of acceptor cations and charge-compensating oxygen vacancies and (ii) the case of a dilute solution of donor cations and charge-compensating electron polarons. In both cases, at high temperatures, the cations (and the charge-compensating defects) are assumed to attain electrochemical equilibrium (this is often termed the Gouy–Chapman case [91,92]), but below a critical temperature T_{crit}, the cations are considered to be immobile, while the charge-compensating defects (oxygen vacancies or electron polarons) remain mobile. The cations, being unable to react to the electrostatic potential, retain the accumulated profile from the Gouy–Chapman case (this we term the restricted equilibrium case [6,25,93]).

On the basis of our atomistic results, we constructed a model that takes all vacancy and acceptor segregation energies (within $d_{gb} \leq 7.5$ Å) into account. In order to determine the importance of taking all sites into account, we also consider a second model, in which all vacancy segregation energies but no acceptor segregation energies were included; a third model, in which only the most negative acceptor and vacancy segregation energies were included; and a fourth model with only the most negative vacancy segregation energy and no acceptor segregation energies. We analyse these cases because, typically, simulations of space-charge layers are set up empirically—the simplest way to describe experimental data in a consistent thermodynamic framework is by taking a single value of $\Delta_{\mathrm{seg}}g_{\mathrm{v}}$ as the driving energy for space-charge layer formation, with $\Delta_{\mathrm{seg}}g_{\mathrm{a}}$ being set to zero.

In Figure 5, we show the obtained values of Φ_0 obtained for the Gd-doped and for the Sc-doped systems. In the case of Gd-doped $\mathrm{CeO_2}$, Φ_0 is positive at all temperatures considered, whereas in the case of Sc-doped $\mathrm{CeO_2}$, it changes from negative to positive (at $T \approx 1667\,\mathrm{K}$). In the Gd-doped case, the third model (with only the most negative $\Delta_{\mathrm{seg}}g_{\mathrm{v}}$ and $\Delta_{\mathrm{seg}}g_{\mathrm{a}}$) shows the smallest deviations from the first model, especially in the restricted-equilibrium regime. It is noteworthy to say this very strong simplification performs better than the case that takes all $\Delta_{\mathrm{seg}}g_{\mathrm{v}}$ into account while omitting the $\Delta_{\mathrm{seg}}g_{\mathrm{a}}$ values. Clearly, acceptor segregation energies play a crucial role for the quantitative description of grain-boundary space-charge layers. Likewise, in Sc-doped $\mathrm{CeO_2}$, the description with only the most negative $\Delta_{\mathrm{seg}}g_{\mathrm{v}}$ and $\Delta_{\mathrm{seg}}g_{\mathrm{a}}$ performs substantially better than the models that disregard $\Delta_{\mathrm{seg}}g_{\mathrm{a}}$, but the deviations are generally larger than in the Gd-doped case.

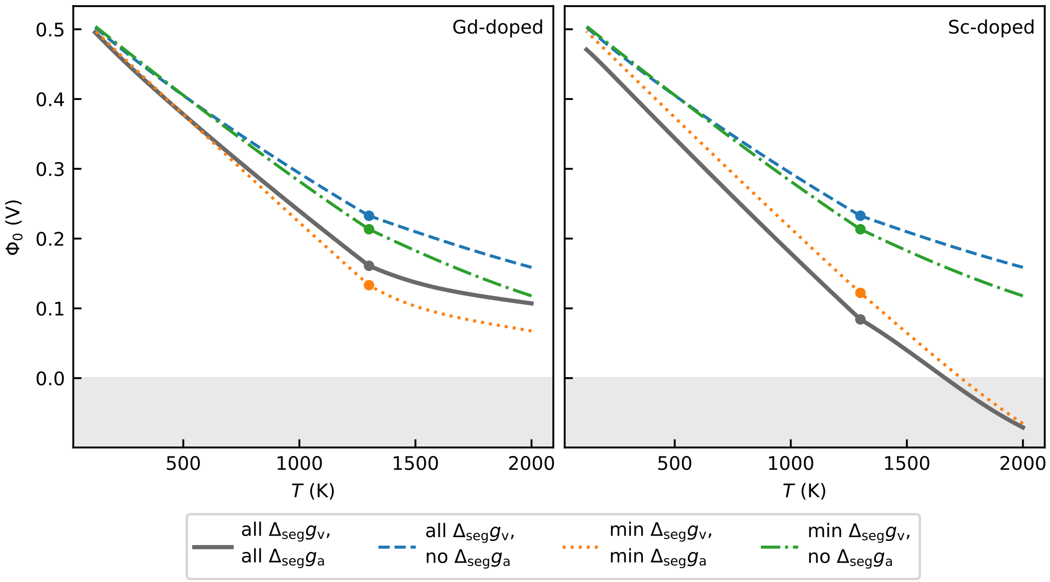

Figure 5. Space-charge potential Φ_0 at the $\Sigma5(310)[001]$ grain boundary calculated as a function of temperature for Gd-doped and for Sc-doped $\mathrm{CeO_2}$ by means of continuum modelling. At high temperatures, Gouy–Chapman behaviour is assumed; below a critical temperature, indicated with a circle, the restricted equilibrium case is assumed.

In order to understand the performance of the different simplified models, we show in Figure 6 the site occupancies within the grain-boundary core, calculated from the first model. Given a specific segregation energy, the occupancies of Ce sites with acceptor cations are generally larger than those of O sites with oxygen vacancies, owing to the positive space-charge potential. The contributions of $\mathrm{v}_{\mathrm{O}}^{\bullet\bullet}$ and $\mathrm{Acc}_{\mathrm{Ce}}'$ to the grain-boundary core charge are, in all considered cases, of the same order of magnitude, and thus, these contributions are much larger than the total grain-boundary core charge. This behaviour may be explained through the levelling effect that the space-charge potential has on both species. The sign of Φ_0 resulting from one of the two species being predominant will serve to decrease the concentration of said species in the core and increase the concentration of the oppositely charged species. Bearing this in mind, one can readily understand why the most negative $\Delta_{\mathrm{seg}}g_{\mathrm{a}}$ must not be disregarded, even when they are smaller in magnitude than the most negative $\Delta_{\mathrm{seg}}g_{\mathrm{v}}$: both defects contribute substantially to the total core charge.

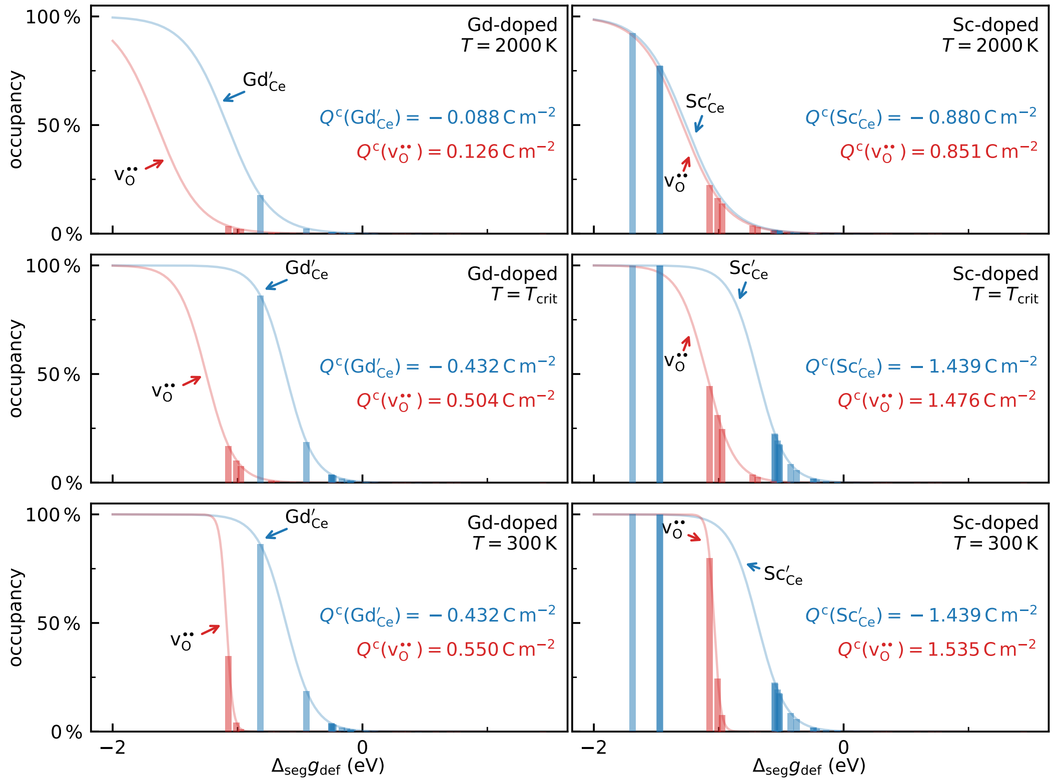

Figure 6. Occupancy of oxygen and cerium grain-boundary core sites with $\mathrm{v}_{\mathrm{O}}^{\bullet\bullet}$ and $\mathrm{Acc}'_{\mathrm{Ce}}$, respectively, calculated from the continuum simulation results according to Equations (5) and (6). The solid lines indicate the functional dependence of the $\mathrm{v}_{\mathrm{O}}^{\bullet\bullet}$ and $\mathrm{Acc}'_{\mathrm{Ce}}$ occupancies as a continuous function of the segregation energy $\Delta_{\mathrm{seg}} g_{\mathrm{def}}$, given the bulk site fractions and the value of Φ_0 taken from the simulation. The partial contributions of $\mathrm{v}_{\mathrm{O}}^{\bullet\bullet}$ and $\mathrm{Acc}'_{\mathrm{Ce}}$ to the overall grain-boundary core charge are given.

It may appear surprising that, in the Sc-doped case, Φ_0 (and Q^{c}) are positive over most of the temperature range, despite the large segregation energies of down to $-1.7\,\mathrm{eV}$ that by far exceed in magnitude the most negative $\mathrm{v}_{\mathrm{O}}^{\bullet\bullet}$ segregation energies. In particular, it is surprising that this sign change takes place within the Gouy–Chapman regime, where a redistribution of acceptor cations from the bulk to the grain-boundary core is possible. This may be explained by the impossibility for a favourable type of site to exceed full occupancy. As indicated by the Fermi–Dirac-type systematics displayed in Figure 6, the grain-boundary core charge would barely be affected if the most favourable types of sites were shifted to even lower energies, since these sites are already fully occupied. Since the areal density of oxygen sites within the grain-boundary core is twice that of cerium sites, and because of the two-fold relative charge of $\mathrm{v}_{\mathrm{O}}^{\bullet\bullet}$, a 100 % occupancy of a specific type of Ce site contributes only as much to Q^{c} as a 25 % occupancy of a specific type of O site. When point-defect segregation energies are obtained from atomistic simulations, one may tend to deduce the sign of the space-charge potential directly from a comparison of the most favourable energies. Our analysis shows that such an approach is not justified; the dependence of the space-charge potential on the set of segregation energies is highly non-trivial.

By considering the occupancies shown in Figure 6, it is also clear why, in the simulations with a scandium dopant, the third model (with only the most negative $\Delta_{\mathrm{seg}} g_{\mathrm{v}}$ and $\Delta_{\mathrm{seg}} g_{\mathrm{a}}$) shows much larger deviations from the simulated behaviour with all sites included than found in the simulations with a gadolinium dopant. At $T = T_{\mathrm{crit}}$ and below, the three most favourable types of Ce sites (with $\Delta_{\mathrm{seg}} g_{\mathrm{a}} = \{-1.69, -1.47, -1.46\}\,\mathrm{eV}$) are all fully occupied, and thus, they all contribute strongly to Q^{c}. None of these sites may be neglected. In the Gd-doped case, even the lowest-energy site (at $\Delta_{\mathrm{seg}} g_{\mathrm{a}} = -0.82\,\mathrm{eV}$) is not fully occupied at T_{crit}, and the sites that are next in energy ($\Delta_{\text{seg}}g_{\text{a}} = \{-0.45, -0.25\}$ eV) are mostly unoccupied.

When space-charge models are set up to explain experimental observations, they are typically formulated on the basis of a single driving energy, $\Delta_{\text{seg}}g_{\text{v}}$, and a corresponding site density Γ_{O}, with a few notable exceptions [9,94]. In such a model, however, $\Delta_{\text{seg}}g_{\text{v}}$ and Γ_{O} do not stand for a single type of site—rather, they represent effective values for the multiplicity of inequivalent sites present in real grain boundaries. It is insufficient, therefore, to simply pick a single value of $\Delta_{\text{seg}}g_{\text{v}}$ and Γ_{O} from atomistic simulations. Rather, the grain-boundary core parameters must be understood as effective parameters, $\Delta_{\text{seg}}g_{\text{v}}^{\text{eff}}$ and $\Gamma_{\text{O}}^{\text{eff}}$. Depending on the set of $\text{v}_{\text{O}}^{\bullet\bullet}$ and Acc'_{Ce} segregation energies, however, such a model need not be able to capture the behaviour of a "full-complexity" model with all segregation energies included. In order to assess how well such a simplification describes the complex behaviour, we fitted a model with a single $\Delta_{\text{seg}}g_{\text{v}}^{\text{eff}}$ value (and $\Delta_{\text{seg}}g_{\text{a}}^{\text{eff}} = 0$) to the $\Phi_0(T)$ data from the full-complexity model, assuming the same critical temperature. In the fit model, both $\Delta_{\text{seg}}g_{\text{v}}$ and Γ_{O} were treated as fit parameters. These results are shown in Figure 7.

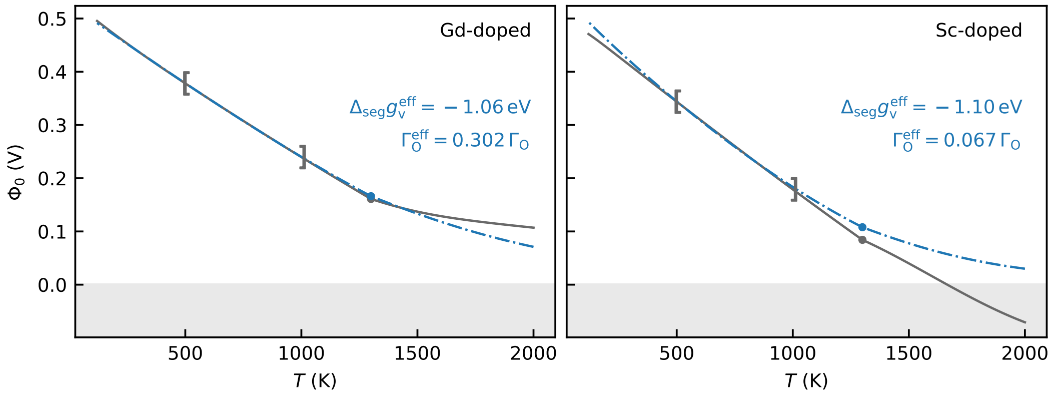

Figure 7. Continuum simulation results (solid line) with all $\Delta_{\text{seg}}g_{\text{v}}$ and $\Delta_{\text{seg}}g_{\text{a}}$ values included, fitted with a model that involves only one $\Delta_{\text{seg}}g_{\text{v}}^{\text{eff}}$ and a corresponding $\Gamma_{\text{O}}^{\text{eff}}$ as fit parameters. At high temperatures, Gouy–Chapman behaviour is assumed; below a critical temperature, indicated with a circle, the restricted equilibrium case is assumed. The simplified model (dash-dotted line) was fitted to the data in the range $[500\,\text{K}, 1000\,\text{K}]$ (as indicated by the brackets) in order to roughly reflect the temperature range in which space-charge potentials are typically obtained from electrical measurement data.

Clearly, the space-charge potentials in the chosen temperature range can be excellently described by a simplified model with only one $\text{v}_{\text{O}}^{\bullet\bullet}$ segregation energy ($\Delta_{\text{seg}}g_{\text{v}}^{\text{eff}}$) and no acceptor segregation energy. In the case of Gd-doped CeO_2, this model extrapolates very well (with deviations $< 6\,\text{mV}$) across the entire considered restricted-equilibrium temperature range (120 K to 1300 K). In the case of Sc-doped CeO_2, the extrapolation is less accurate (with deviations up to 24 mV) but still very good. In both cases, an extrapolation from the restricted-equilibrium range to the behaviour in the Gouy–Chapman regime is very inaccurate; in the Sc-doped case, it even leads to a false prediction of the sign of Φ_0 at high temperatures. The effective segregation energies obtained from the fit are, in both cases, remarkably close to the most negative segregation energy ($\Delta_{\text{seg}}g_{\text{v}} = -1.07\,\text{eV}$) included in the simulations, thus demonstrating again how space-charge behaviour is dominated by the most negative segregation energies, rather than by an average of segregation energies. The effective areal site densities are substantially lower than the individual site density Γ_{O} of each symmetry-inequivalent oxygen site. And the effective site density is much lower in the Sc-doped case than in the Gd-doped case ($0.07\,\Gamma_{\text{O}}$ compared to $0.3\,\Gamma_{\text{O}}$). This can be attributed to the much more negative $\Delta_{\text{seg}}g_{\text{a}}$ for scandium ions than for gadolinium ions: as shown in Figure 6, there are generally more highly occupied grain-boundary cation sites in the Sc-doped case, and thus, a larger negative contribution to the grain-boundary core charge. As a consequence of this large negative counter-charge, the occupancies of oxygen sites with $v_O^{\bullet\bullet}$ can also become larger, leaving a much smaller fraction of the oxygen sites to be unoccupied. In a model that disregards the acceptor segregation energies, this smaller fraction of available oxygen sites has the appearance of a smaller oxygen-site density.

An even simpler analysis can be performed by assuming the Mott–Schottky case, that is, ignoring the accumulated dopant profile. In this case, the segregation energies are again obtained quite accurately (not shown), but the effective site densities are even lower (by ∼40% in the Gd-doped case and by ∼20% in the Sc-doped case) than in the fit of the restricted equilibrium model.

Having examined in detail the effects of multiple segregation energies in acceptor-doped CeO_2, we now turn to donor-doped CeO_2. In Figure 8, we show values of $\Phi_0(T)$ obtained for Ta-doped CeO_2, assuming that the $Ta_{Ce}^{\bullet}$ donor cations are compensated by electron polarons ($n_e = n_d$). At high temperatures, we find positive space-charge potentials, originating in the strongly negative $Ta_{Ce}^{\bullet}$ segregation energies (down to -2.4 eV). In the restricted-equilibrium regime, Φ_0 decreases strongly with decreasing temperature and changes sign at $T = 698$ K, indicating that Ce_{Ce}' segregation becomes dominant owing to the $Ta_{Ce}^{\bullet}$ ions' inability to further segregate to the grain-boundary core. This behaviour suggests that in a sample with the considered defect chemistry, the space-charge contribution to the grain-boundary resistivity should vanish abruptly above a threshold temperature, owing to the space-charge layer's changing character, from depleted mobile charge carriers (electron polarons) at low temperatures to accumulated mobile charge carriers at high temperatures.

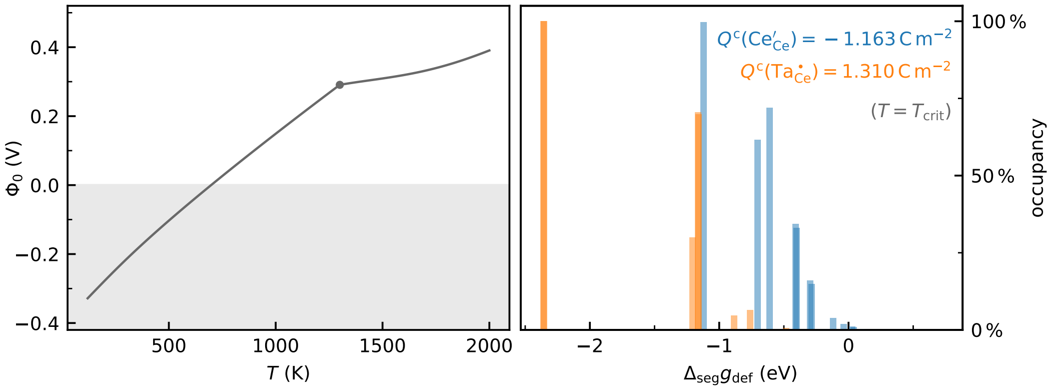

Figure 8. Space-charge potential Φ_0 (**left**) and grain-boundary core site occupancies (**right**) at the $\Sigma5(310)[001]$ grain boundary calculated as a function of temperature for Ta-doped CeO_2 by means of continuum modelling. At high temperatures, Gouy–Chapman behaviour is assumed; below a critical temperature, indicated with a circle, the restricted equilibrium case is assumed.

4. Conclusions

In this study, we investigated various aspects concerning the formation of space-charge layers at a grain boundary in fluorite-structured CeO_2. First, at the atomistic level, we examined how to define the structural grain-boundary width, and how the segregation energetics are related to simple structural descriptors. For this, we employed classical Molecular Statics (MS) and Molecular Dynamics (MD) simulations. We then analysed, by means of Finite Element Method (FEM) continuum simulations of a dilute solid solution, how the behaviour of the space-charge potential is affected by the variety of segregation energies. As answers to these questions we obtained the following:

1. The segregation energetics of point defects, the interatomic distances, and the coordination numbers all exhibit a similar length scale on which they deviate from bulk values. Although the precise cutoff between bulk and grain-boundary regions is somewhat arbitrary, all three quantities yield for this grain boundary in this system a grain-boundary width of ca. 7.5 Å on either side of the interface, i.e., ca. 1.5 nm in total.

2. Even for a symmetric, tilt grain boundary, there is no clear relationship between simple structural descriptors (such as the ionic size mismatch, nearest-neighbour distances, and effective coordination numbers) and defect energetics.
3. In a space-charge model, most segregation energies (especially the positive values) can safely be neglected and the complexity of the model can in this manner be strongly reduced. To avoid oversimplification, however, one must consider that (i) a correct prediction of the $\Phi_0(T)$ behaviour (both quantitatively and qualitatively) can only be achieved if site-exclusion effects are taken into account; (ii) segregation energies for acceptors ($\Delta_{\text{seg}}g_{\text{a}}$) must not be disregarded, even though the sign of Φ_0 is in most cases governed by oxygen-vacancy segregation, rather than by acceptor segregation; (iii) when a simple, empirical space-charge model (with $\Delta_{\text{seg}}g_{\text{a}} = 0$) is fitted to experimental data, the obtained grain-boundary parameters ($\Delta_{\text{seg}}g_{\text{V}}$ and $\Gamma^{\text{c}}_{\text{O}}$) are *effective* values that are not directly comparable to atomistic results since they incorporate the effects of acceptor segregation. Nevertheless, in our model system, we found such a fit to yield good estimates of $\Delta_{\text{seg}}g_{\text{V}}$ together with good extrapolating capabilities of the $\Phi_0(T)$ behaviour within the restricted-equilibrium regime.

These results highlight that for a rational design of the grain-boundary electrical properties in ceramics, purely structural considerations are hardly informative. More than that, even atomistic calculations of segregation energies will be insufficient, unless they serve as the basis for a detailed space-charge model. In this study, we have laid out the degree of detail that such a model requires in order to yield meaningful results.

Author Contributions: A.L.U.: Atomistic simulations, Continuum simulations, Structural analysis, Visualisation, Writing—original draft preparation, Writing—review & editing. H.J.H.: Atomistic simulations, Structural analysis, Writing—review & editing. R.A.D.S.: Conceptualization, Project administration, Supervision, Writing—original draft preparation, Writing—review & editing, Funding acquisition. A.R.G.-S.: Atomistic simulations, Project administration, Supervision, Writing—original draft preparation, Writing—review & editing. All authors have read and agreed to the published version of the manuscript.

Funding: Financial support from the German Science Foundation (DFG) within the framework of the collaborative research centre 'Nanoswitches' (SFB 917, Project No. 167917811) and within the Priority Programme (SPP1959, Project No. 319339707) 'Fields-Matter' under project DE 2854/9-2 is gratefully acknowledged.

Data Availability Statement: Data are available from the authors upon reasonable request.

Acknowledgments: The authors thank Matthew J. Wolf and Alexander Bonkowski for fruitful discussions. Simulations were performed with computing resources granted by RWTH Aachen University under project rwth0189 and by JARA-HPC from RWTH Aachen University under project jara0100.

Conflicts of Interest: The authors declare no conflicts of interest. The funders had no role in the design of the study; in the collection, analyses, or interpretation of data; in the writing of the manuscript; or in the decision to publish the results.

References

1. Feighery, A.J.; Irvine, J.T.S. Effect of alumina additions upon electrical properties of 8 mol% yttria-stabilised zirconia. *Solid State Ion.* **1999**, *121*, 209–216. [CrossRef]
2. Cho, Y.H.; Cho, P.S.; Auchterlonie, G.; Kim, D.K.; Lee, J.H.; Kim, D.Y.; Park, H.M.; Drennan, J. Enhancement of grain-boundary conduction in gadolinia-doped ceria by the scavenging of highly resistive siliceous phase. *Acta Mater.* **2007**, *55*, 4807–4815. [CrossRef]
3. Yan, M.; Luo, S.D.; Schaffer, G.B.; Qian, M. Impurity (Fe, Cl, and P)-Induced Grain Boundary and Secondary Phases in Commercially Pure Titanium (CP-Ti). *Metall. Mater. Trans. A* **2013**, *44*, 3961–3969. [CrossRef]
4. Tschoepe, A.; Birringer, R. Grain size dependence of electrical conductivity in polycrystalline cerium oxide. *J. Electroceram.* **2001**, *7*, 169–177. [CrossRef]
5. Guo, X.; Maier, J. Grain Boundary Blocking Effect in Zirconia: A Schottky Barrier Analysis. *J. Electrochem. Soc.* **2001**, *148*, E121. [CrossRef]

6. De Souza, R.A. The formation of equilibrium space-charge zones at grain boundaries in the perovskite oxide $SrTiO_3$. *Phys. Chem. Chem. Phys.* **2009**, *11*, 9939–9969. [CrossRef] [PubMed]
7. Guo, X.; Waser, R. Space charge concept for acceptor-doped zirconia and ceria and experimental evidences. *Solid State Ion.* **2004**, *173*, 63–67. [CrossRef]
8. Tong, X.; Mebane, D.S.; De Souza, R.A. Analyzing the grain-boundary resistance of oxide-ion conducting electrolytes: Poisson-Cahn vs. Poisson-Boltzmann theories. *J. Am. Ceram. Soc.* **2019**, *103*, 5–22. [CrossRef]
9. Helgee, E.E.; Lindman, A.; Wahnstrom, G. Origin of Space Charge in Grain Boundaries of Proton-Conducting $BaZrO_3$. *Fuel Cells* **2013**, *13*, 19–28. [CrossRef]
10. Shirpour, M.; Merkle, R.; Maier, J. Space charge depletion in grain boundaries of $BaZrO_3$ proton conductors. *Solid State Ion.* **2012**, *225*, 304–307. [CrossRef]
11. Gellert, M.; Gries, K.I.; Yada, C.; Rosciano, F.; Volz, K.; Roling, B. Grain Boundaries in a Lithium Aluminum Titanium Phosphate-Type Fast Lithium Ion Conducting Glass Ceramic: Microstructure and Nonlinear Ion Transport Properties. *J. Phys. Chem. C* **2012**, *116*, 22675–22678. [CrossRef]
12. Genreith-Schriever, A.R.; Parras, J.P.; Heelweg, H.J.; De Souza, R.A. The Intrinsic Structural Resistance of a Grain Boundary to Transverse Ionic Conduction. *ChemElectroChem* **2020**, *7*, 4718–4723. [CrossRef]
13. Tuller, H.L.; Nowick, A.S. Small Polaron Electron-Transport in Reduced CeO_2 Single-Crystals. *J. Phys. Chem. Solids* **1977**, *38*, 859–867. [CrossRef]
14. Steele, B. Appraisal of $Ce_{1-y}Gd_yO_{2-y/2}$ electrolytes for IT-SOFC operation at 500 °C. *Solid State Ion.* **2000**, *129*, 95–110. [CrossRef]
15. Fuentes, R.O.; Baker, R.T. Synthesis and properties of Gadolinium-doped ceria solid solutions for IT-SOFC electrolytes. *Int. J. Hydrog. Energy* **2008**, *33*, 3480–3484. [CrossRef]
16. Shajahan, I.; Ahn, J.; Nair, P.; Medisetti, S.; Patil, S.; Niveditha, V.; Uday Bhaskar Babu, G.; Dasari, H.P.; Lee, J.H. Praseodymium doped ceria as electrolyte material for IT-SOFC applications. *Mater. Chem. Phys.* **2018**, *216*, 136–142. [CrossRef]
17. Wang, D.Y.; Nowick, A.S. The Grain-Boundary Effect in Doped Ceria Solid Electrolytes. *J. Solid State Chem.* **1980**, *35*, 325–333. [CrossRef]
18. Gerhardt, R.; Nowick, A.S. Grain-boundary effect in ceria doped with trivalent cations: I, electrical measurements. *J. Am. Ceram. Soc.* **1986**, *69*, 641–646. [CrossRef]
19. Gerhardt, R.; Nowick, A.S.; Mochel, M.E.; Dumler, I. Grain-boundary effect in ceria doped with trivalent cations: II, Microstructure and microanalysis. *J. Am. Ceram. Soc.* **1986**, *69*, 647–651. [CrossRef]
20. Tanaka, J.; Baumard, J.F.; Abelard, P. Nonlinear electrical properties of grain boundaries in an oxygen-ion conductor ($CeO_2 \cdot Y_2O_3$). *J. Am. Ceram. Soc.* **1987**, *70*, 637–643. [CrossRef]
21. Christie, G.M.; Van Berkel, F.P.F. Microstructure–ionic conductivity relationships in ceria-gadolinia electrolytes. *Solid State Ion.* **1996**, *83*, 17–27. [CrossRef]
22. Aoki, M.; Chiang, Y.M.; Kosacki, I.; Lee, L.J.R.; Tuller, H.; Liu, Y. Solute Segregation and Grain-Boundary Impedance in High-Purity Stabilized Zirconia. *J. Am. Ceram. Soc.* **1996**, *79*, 1169–1180. [CrossRef]
23. Guo, X.; Sigle, W.; Maier, J. Blocking grain boundaries in yttria-doped and undoped ceria ceramics of high purity. *J. Am. Ceram. Soc.* **2003**, *86*, 77–87. [CrossRef]
24. Tschoepe, A. Grain size-dependent electrical conductivity of polycrystalline cerium oxide II: Space charge model. *Solid State Ion.* **2001**, *139*, 267–280. [CrossRef]
25. Tschoepe, A.; Kilassonia, S.; Birringer, R. The grain boundary effect in heavily doped cerium oxide. *Solid State Ion.* **2004**, *173*, 57–61. [CrossRef]
26. Mebane, D.S.; De Souza, R.A. A generalised space-charge theory for extended defects in oxygen-ion conducting electrolytes: From dilute to concentrated solid solutions. *Energy Environ. Sci.* **2015**, *8*, 2935–2940. [CrossRef]
27. Parras, J.P.; Cao, C.; Ma, Z.; Mücke, R.; Jin, L.; Dunin-Borkowski, R.; Guillon, O.; De Souza, R.A. The grain-boundary resistance of CeO_2 ceramics: A combined microscopy–spectroscopy–simulation study of a dilute solution. *J. Am. Ceram. Soc.* **2020**, *103*, 1755–1764. [CrossRef]
28. Lei, Y.; Ito, Y.; Browning, N.D.; Mazanec, T.J. Segregation Effects at Grain Boundaries in Fluorite-Structured Ceramics. *J. Am. Ceram. Soc.* **2002**, *85*, 2359–2363. [CrossRef]
29. Hojo, H.; Mizoguchi, T.; Ohta, H.; Findlay, S.D.; Shibata, N.; Yamamoto, T.; Ikuhara, Y. Atomic Structure of a CeO_2 Grain Boundary: The Role of Oxygen Vacancies. *Nano Lett.* **2010**, *10*, 4668–4672. [CrossRef] [PubMed]
30. Lee, W.; Jung, H.J.; Lee, M.H.; Kim, Y.B.; Park, J.S.; Sinclair, R.; Prinz, F.B. Oxygen surface exchange at grain boundaries of oxide ion conductors. *Adv. Funct. Mater.* **2012**, *22*, 965–971. [CrossRef]
31. Lee, H.B.; Prinz, F.B.; Cai, W. Atomistic simulations of grain boundary segregation in nanocrystalline yttria-stabilized zirconia and gadolinia-doped ceria solid oxide electrolytes. *Acta Mater.* **2013**, *61*, 3872–3887. [CrossRef]
32. Parras, J.P.; De Souza, R.A. Grain-boundary diffusion of cations in fluorite-type oxides is faster but not always easier. *Acta Mater.* **2020**, *195*, 383–391. [CrossRef]
33. Beschnitt, S.; De Souza, R.A. Impurity diffusion of Hf and Zr in Gd-doped CeO_2. *Solid State Ion.* **2017**, *305*, 23–29. [CrossRef]
34. Aidhy, D.S.; Zhang, Y.W.; Weber, W.J. Impact of segregation energetics on oxygen conductivity at ionic grain boundaries. *J. Mater. Chem. A* **2014**, *2*, 1704–1709. [CrossRef]

35. Arora, G.; Aidhy, D.S. Segregation and binding energetics at grain boundaries in fluorite oxides. *J. Mater. Chem. A* **2017**, *5*, 4026–4035. [CrossRef]
36. Wu, L.; Aguiar, J.A.; Dholabhai, P.P.; Holesinger, T.; Aoki, T.; Uberuaga, B.P.; Castro, R.H. Interface energies of nanocrystalline doped ceria: Effects of manganese segregation. *J. Phys. Chem. C* **2015**, *119*, 27855–27864. [CrossRef]
37. Yuan, F.; Liu, B.; Zhang, Y.; Weber, W.J. Segregation and Migration of the Oxygen Vacancies in the $\Sigma3$ (111) Tilt Grain Boundaries of Ceria. *J. Phys. Chem. C* **2016**, *120*, 6625–6632. [CrossRef]
38. Symington, A.R.; Molinari, M.; Statham, J.; Wu, J.; Parker, S.C. The role of dopant segregation on the oxygen vacancy distribution and oxygen diffusion in CeO_2 grain boundaries. *JPhys Energy* **2019**, *1*, 042005. [CrossRef]
39. Fisher, C.A.J.; Matsubara, H. Molecular dynamics investigations of grain boundary phenomena in cubic zirconia. *Comput. Mater. Sci.* **1999**, *14*, 177–184. [CrossRef]
40. Mao, Z.G.; Sinnott, S.B.; Dickey, E.C. Ab initio calculations of pristine and doped zirconia $\Sigma5(310)/[001]$ tilt grain boundaries. *J. Am. Ceram. Soc.* **2002**, *85*, 1594–1600. [CrossRef]
41. Oyama, T.; Yoshiya, M.; Matsubara, H.; Matsunaga, K. Numerical analysis of solute segregation at Σ 5(310)/[001] symmetric tilt grain boundaries in Y_2O_3-doped ZrO_2. *Phys. Rev. B* **2005**, *71*, 224105. [CrossRef]
42. Nerikar, P.V.; Rudman, K.; Desai, T.G.; Byler, D.; Unal, C.; McClellan, K.J.; Phillpot, S.R.; Sinnott, S.B.; Peralta, P.; Uberuaga, B.P.; et al. Grain Boundaries in Uranium Dioxide: Scanning Electron Microscopy Experiments and Atomistic Simulations. *J. Am. Ceram. Soc.* **2011**, *94*, 1893–1900. [CrossRef]
43. Yoshiya, M.; Oyama, T. Impurity and vacancy segregation at symmetric tilt grain boundaries in Y_2O_3-doped ZrO_2. *J. Mater. Sci.* **2011**, *46*, 4176–4190. [CrossRef]
44. Hong, M.K.; Uberuaga, B.P.; Phillpot, S.R.; Andersson, D.A.; Stanek, C.R.; Sinnott, S.B. The role of charge and ionic radius on fission product segregation to a model UO_2 grain boundary. *J. Appl. Phys.* **2013**, *113*. [CrossRef]
45. Williams, N.R.; Molinari, M.; Parker, S.C.; Storr, M.T. Atomistic investigation of the structure and transport properties of tilt grain boundaries of UO_2. *J. Nucl. Mater.* **2015**, *458*, 45–55. [CrossRef]
46. Dholabhai, P.P.; Aguiar, J.A.; Wu, L.J.; Holesinger, T.G.; Aoki, T.; Castro, R.H.R.; Uberuaga, B.P. Structure and segregation of dopant-defect complexes at grain boundaries in nanocrystalline doped ceria. *Phys. Chem. Chem. Phys.* **2015**, *17*, 15375–15385. [CrossRef] [PubMed]
47. Feng, B.; Sugiyama, I.; Hojo, H.; Ohta, H.; Shibata, N.; Ikuhara, Y. Atomic structures and oxygen dynamics of CeO_2 grain boundaries. *Sci. Rep.* **2016**, *6*, 20288. [CrossRef] [PubMed]
48. Usler, A.L.; Ketter, F.; De Souza, R.A. How space-charge behaviour at grain boundaries in electroceramic oxides is modified by two restricted equilibria. *Phys. Chem. Chem. Phys.* **2024**, *26*, 8287–8298. [CrossRef] [PubMed]
49. Hagege, S.; Carter, C.B.; Cosandey, F.; Sass, S.L. The variation of grain boundary structural width with misorientation angle and boundary plane. *Phil. Mag. A* **1982**, *45*, 723–740. [CrossRef]
50. Wynblatt, P.; Rohrer, G.S.; Papillon, F. Grain boundary segregation in oxide ceramics. *J. Eur. Ceram. Soc.* **2003**, *23*, 2841–2848. [CrossRef]
51. Kingery, W.D. Plausible Concepts Necessary and Sufficient for Interpretation of Ceramic Grain-Boundary Phenomena-II, Solute Segregation, Grain-Boundary Diffusion, and General Discussion. *J. Am. Ceram. Soc.* **1974**, *57*, 74–83. [CrossRef]
52. Kingery, W.D. Segregation phenomena at surfaces and at grain boundaries in oxides and carbides. *Solid State Ion.* **1984**, *12*, 299–307. [CrossRef]
53. Avila-Paredes, H.J.; Choi, K.; Chen, C.T.; Kim, S. Dopant-concentration dependence of grain-boundary conductivity in ceria: A space-charge analysis. *J. Mater. Chem.* **2009**, *19*, 4837–4842. [CrossRef]
54. Vollman, M.; Waser, R. Grain Boundary Defect Chemistry of Acceptor-Doped Titanates: Space Charge Layer Width. *J. Am. Ceram. Soc.* **1994**, *77*, 235–243. [CrossRef]
55. Peterson, N.L. Grain-boundary diffusion in metals. *Int. Met. Rev.* **1983**, *28*, 65–91. [CrossRef]
56. Mistler, R.E.; Coble, R.L. Grain-boundary diffusion and boundary widths in metals and ceramics. *J. Appl. Phys.* **1974**, *45*, 1507–1509. [CrossRef]
57. Zacherle, T.; Schriever, A.; De Souza, R.A.; Martin, M. Ab initio analysis of the defect structure of ceria. *Phys. Rev. B* **2013**, *87*, 134104-1–134104-11. [CrossRef]
58. Tuller, H.L.; Nowick, A.S. Doped ceria as a solid oxide electrolyte. *J. Electrochem. Soc.* **1975**, *122*, 255. [CrossRef]
59. Tuller, H.L.; Nowick, A.S. Defect Structure and Electrical-Properties of Nonstoichiometric CeO_2 Single-Crystals. *J. Electrochem. Soc.* **1979**, *126*, 209–217. [CrossRef]
60. Stratton, T.G.; Tuller, H.L. Thermodynamic and transport studies of mixed oxides. The CeO_2–UO_2 system. *J. Chem. Soc. Faraday Trans. 2* **1987**, *83*, 1143–1156. [CrossRef]
61. Göbel, M.C.; Gregori, G.; Maier, J. Electronically blocking grain boundaries in donor doped cerium dioxide. *Solid State Ion.* **2012**, *215*, 45–51. [CrossRef]
62. Waldow, S.P.; Wardenga, H.; Beschnitt, S.; Klein, A.; De Souza, R.A. Concentration and Diffusivity of Oxygen Interstitials in Niobia-Doped Ceria. *J. Phys. Chem. C* **2019**, *123*, 6340–6350. [CrossRef]
63. Kröger, F.; Vink, H. Relations between the concentrations of imperfections in crystalline solids. *Solid State Phys.* **1956**, *3*, 307–435. [CrossRef]

64. Norby, T. A Kröger–Vink compatible notation for defects in inherently defective sublattices. *J. Korean Ceram. Soc.* **2010**, *47*, 19–25. [CrossRef]
65. De Souza, R.; Harrington, G. Revisiting point defects in ionic solids and semiconductors. *Nat. Mater.* **2023**, *22*, 794–797. [CrossRef] [PubMed]
66. Born, M.; Mayer, J.E. Zur Gittertheorie der Ionenkristalle. *Z. Phys.* **1932**, *75*, 1–18. [CrossRef]
67. Balducci, G.; Kaspar, J.; Fornasiero, P.; Graziani, M.; Islam, M.S.; Gale, J.D. Computer simulation studies of bulk reduction and oxygen migration in CeO_2-ZrO_2 solid solutions. *J. Phys. Chem. B* **1997**, *101*, 1750–1753. [CrossRef]
68. Lewis, G.V.; Catlow, C.R.A. Potential models for ionic oxides. *J. Phys. C Solid State Phys.* **1985**, *18*, 1149. [CrossRef]
69. Exner, M.; Donnerberg, H.; Catlow, C.R.A.; Schirmer, O.F. Computer simulation of defects in $KTaO_3$. *Phys. Rev. B* **1995**, *52*, 3930. [CrossRef] [PubMed]
70. Sayle, T.X.T.; Parker, S.C.; Sayle, D.C. Oxidising CO to CO_2 using ceria nanoparticles. *Phys. Chem. Chem. Phys.* **2005**, *7*, 2936–2941. [CrossRef] [PubMed]
71. Sayle, T.X.T.; Parker, S.C.; Sayle, D.C. Ionic conductivity in nano-scale CeO_2/YSZ heterolayers. *J. Mater. Chem.* **2006**, *16*, 1067–1081. [CrossRef]
72. Sayle, T.X.T.; Parker, S.C.; Sayle, D.C. Oxygen transport in unreduced, reduced and Rh(III)-doped CeO_2 nanocrystals. *Faraday Disc.* **2007**, *134*, 377–397. [CrossRef] [PubMed]
73. De Souza, R.A.; Metlenko, V.; Park, D.; Weirich, T.E. Behavior of oxygen vacancies in single-crystal $SrTiO_3$: Equilibrium distribution and diffusion kinetics. *Phys. Rev. B* **2012**, *85*, 174109. [CrossRef]
74. Plimpton, S. Fast Parallel Algorithms for Short-Range Molecular-Dynamics. *J. Comput. Phys.* **1995**, *117*, 1–19. [CrossRef]
75. Wojdyr, M.; Khalil, S.; Liu, Y.; Szlufarska, I. Energetics and structure of (001) tilt grain boundaries in SiC. *Model. Simul. Mater. Sci. Eng.* **2010**, *18*, 075009. [CrossRef]
76. Yang, L.; Wirth, B.D. Tilt grain boundary stability in uranium dioxide and effect on xenon segregation. *J. Nucl. Mater.* **2023**, *577*, 154302. [CrossRef]
77. Heinz, M.V.; Usler, A.L.; Bonkowski, A.; Feldmann, G. Molara. 2024. Available online: https://zenodo.org/records/11120926 (accessed on 7 May 2024).
78. Hoppe, R.; Mehlhorn, B. Die Kristallstruktur von K_2ZrF_6. *Z. Anorg. Allg. Chem.* **1976**, *425*, 200–208. [CrossRef]
79. Hoppe, R. Effective coordination numbers (ECoN) and mean fictive ionic radii (MEFIR). *Z. Für Krist.-Cryst. Mater.* **1979**, *150*, 23–52. [CrossRef]
80. Bentley, J.L. Multidimensional binary search trees used for associative searching. *Commun. ACM* **1975**, *18*, 509–517. [CrossRef]
81. Virtanen, P.; Gommers, R.; Oliphant, T.E.; Haberland, M.; Reddy, T.; Cournapeau, D.; Burovski, E.; Peterson, P.; Weckesser, W.; Bright, J.; et al. SciPy 1.0: Fundamental Algorithms for Scientific Computing in Python. *Nat. Methods* **2020**, *17*, 261–272. [CrossRef] [PubMed]
82. Pan, H.; Ganose, A.M.; Horton, M.; Aykol, M.; Persson, K.A.; Zimmermann, N.E.R.; Jain, A. Benchmarking coordination number prediction algorithms on inorganic crystal structures. *Inorg. Chem.* **2021**, *60*, 1590–1603. [CrossRef] [PubMed]
83. Brauer, G.; Gingerich, K.; Holtschmidt, U. Über die Oxyde des Cers-IV: Die Sauerstoffzersetzungdrücke im System der Ceroxyde. *J. Inorg. Nucl. Chem.* **1960**, *16*, 77–86. [CrossRef]
84. Shirpour, M.; Gregori, G.; Merkle, R.; Maier, J. On the proton conductivity in pure and gadolinium doped nanocrystalline cerium oxide. *Phys. Chem. Chem. Phys.* **2011**, *13*, 937–940. [CrossRef] [PubMed]
85. Nerikar, P.V.; Parfitt, D.C.; Trujillo, L.A.C.; Andersson, D.A.; Unal, C.; Sinnott, S.B.; Grimes, R.W.; Uberuaga, B.P.; Stanek, C.R. Segregation of xenon to dislocations and grain boundaries in uranium dioxide. *Phys. Rev. B* **2011**, *84*. [CrossRef]
86. Tao, C.; Mutter, D.; Urban, D.F.; Elsässer, C. Atomistic calculations of charged point defects at grain boundaries in $SrTiO_3$. *Phys. Rev. B* **2021**, *104*, 054114. [CrossRef]
87. Shannon, R.D. Revised Effective Ionic-Radii and Systematic Studies of Interatomic Distances in Halides and Chalcogenides. *Acta Cryst. A* **1976**, *32*, 751–767. [CrossRef]
88. Tschoepe, A. Interface defect chemistry and effective conductivity in polycrystalline cerium oxide. *J. Electroceram.* **2005**, *14*, 5–23. [CrossRef]
89. Guo, X.; Waser, R. Electrical properties of the grain boundaries of oxygen ion conductors: Acceptor-doped zirconia and ceria. *Prog. Mater. Sci.* **2006**, *51*, 151–210. [CrossRef]
90. McCune, R.C.; Wynblatt, P. Calcium segregation to a magnesium oxide (100) surface. *J. Am. Ceram. Soc.* **1983**, *66*, 111–117. [CrossRef]
91. Gouy, M. Sur la constitution de la charge électrique à la surface d'un électrolyte. *J. Phys. Theor. Appl.* **1910**, *9*, 457–468. [CrossRef]
92. Chapman, D.L. A contribution to the theory of electrocapillarity. *Lond. Edinb. Dublin Philos. Mag. J. Sci.* **1913**, *25*, 475–481. [CrossRef]
93. Lee, J.S.; Kim, D.Y. Space-charge concepts on grain boundary impedance of a high-purity yttria-stabilized tetragonal zirconia polycrystal. *J. Mater. Res.* **2001**, *16*, 2739–2751. [CrossRef]
94. Lindman, A.; Helgee, E.E.; Nyman, B.J.; Wahnström, G. Oxygen vacancy segregation in grain boundaries of $BaZrO_3$ using interatomic potentials. *Solid State Ion.* **2013**, *230*, 27–31. [CrossRef]

Disclaimer/Publisher's Note: The statements, opinions and data contained in all publications are solely those of the individual author(s) and contributor(s) and not of MDPI and/or the editor(s). MDPI and/or the editor(s) disclaim responsibility for any injury to people or property resulting from any ideas, methods, instructions or products referred to in the content.